PNAS RESEARCH ARTICLE | BIOPHYSICS AND COMPUTATIONAL BIOLOGY OPEN ACCESS

Topological crossing in the misfolded *Tetrahymena* ribozyme resolved by cryo-EM

Shanshan Li[a,b], Michael Z. Palo[c], Grigore Pintilie[b], Xiaojing Zhang[a], Zhaoming Su[b,d], Kalli Kappel[c], Wah Chiu[b,e,1], Kaiming Zhang[a,b,1], and Rhiju Das[c,f,1]

Edited by Hongwei Wang, Tsinghua University, Beijing, China; received May 26, 2022; accepted August 9, 2022 by Editorial Board Member Yifan Cheng

The *Tetrahymena* group I intron has been a key system in the understanding of RNA folding and misfolding. The molecule folds into a long-lived misfolded intermediate (M) *in vitro*, which has been known to form extensive native-like secondary and tertiary structures but is separated by an unknown kinetic barrier from the native state (N). Here, we used cryogenic electron microscopy (cryo-EM) to resolve misfolded structures of the *Tetrahymena* L-21 ScaI ribozyme. Maps of three M substates (M1, M2, M3) and one N state were achieved from a single specimen with overall resolutions of 3.5 Å, 3.8 Å, 4.0 Å, and 3.0 Å, respectively. Comparisons of the structures reveal that all the M substates are highly similar to N, except for rotation of a core helix P7 that harbors the ribozyme's guanosine binding site and the crossing of the strands J7/3 and J8/7 that connect P7 to the other elements in the ribozyme core. This topological difference between the M substates and N state explains the failure of 5′-splice site substrate docking in M, supports a topological isomer model for the slow refolding of M to N due to a trapped strand crossing, and suggests pathways for M-to-N refolding.

Tetrahymena ribozyme | misfolded | cryo-EM

Significance

Taking advantage of single-particle cryogenic electron microscopy (cryo-EM) to analyze highly heterogeneous or flexible samples, we obtained long-awaited three-dimensional (3D) structures of the misfolded *Tetrahymena* ribozyme. These structures provide clear evidence for a previously proposed topological isomer model, in which the stereochemically impossible crossing of two core RNA strands prevents rapid rearrangement of the misfolded state to the native state. Topological isomers may be widespread in misfolding of complex RNA, and these cryo-EM structures set a foundation for dissecting their detailed kinetic mechanisms and functional consequences in a paradigmatic model system.

The *Tetrahymena thermophila* group I self-splicing intron was the first RNA-only system to be identified as a catalytic RNA (1). RNAs need to be precisely folded into specific three-dimensional (3D) structures to function in biological processes such as protein translation and splicing but appear highly susceptible to misfolding (2). Like many structured RNAs, the *Tetrahymena* ribozyme assembles via a variety of folding pathways, many of which end up in nonnative kinetic traps (3). Under standard conditions *in vitro*, a small fraction folds to the native (N) state within 1 min, while the remaining fraction forms a long-lived misfolded intermediate (M) that refolds to the N state on a time scale of hours (3–5). The structural mechanism of this conformational switch remains unknown.

The N state comprises an intricate catalytic core involving numerous strands and helices that bind the substrates of the splicing reaction along with an extensive ring of peripheral elements that "locks in" this core (6). Biochemical data indicate that the secondary and tertiary structures of M bear a close resemblance to N. Nevertheless, it has remained paradoxical that the transition from M to N is so slow when the states are so structurally similar to each other. A potential resolution to the paradox comes from a proposal that M and N are topologically distinct, with at least one pair of strands crossed in the core (7). The transition from the M state to the N state then cannot occur through a fast local rearrangement because of stereochemical constraints but instead requires unfolding of the ribozyme's peripheral regions to release constraints on movement of core elements. Rearrangements of relative positions of core strands and helices in this unlocked state lead to the native-like topology, after which refolding of the peripheral tertiary contacts locks in the N state (3, 7–10). While this topological model is compelling and consistent with a wealth of biochemical data, the 3D structure of M has not been resolved, and it remains unknown which, if any, of the possible strand topological crossings are present in M.

Here, we performed single-particle cryogenic electron microscopy (cryo-EM) to obtain structures of the M and N states. The structures provide unequivocal evidence for the topological isomer model, explain a large body of prior biochemical data and, by pinpointing a specific topological crossing, suggest possible pathways for transition from M to N. Our results illustrate the growing ability of cryo-EM to reveal complex structural changes in RNA folding pathways.

Results

Single-Particle Cryo-EM Analysis. To visualize the M state of the *Tetrahymena* ribozyme, we folded the L-21 ScaI ribozyme by adding 10 mM Mg^{2+} to the RNA prepared in a

Author contributions: S.L., M.Z.P., W.C., K.Z., and R.D. designed research; S.L., M.Z.P., X.Z., and K.Z. performed research; S.L., M.Z.P., G.P., Z.S., K.K., W.C., K.Z., and R.D. analyzed data; and S.L., M.Z.P., W.C., K.Z., and R.D. wrote the paper.

The authors declare no competing interest.

This article is a PNAS Direct Submission. H.W. is a guest editor invited by the Editorial Board.

[1]To whom correspondence may be addressed. Email: wahc@stanford.edu or kmzhang@ustc.edu.cn or rhiju@stanford.edu.

This article contains supporting information online at http://www.pnas.org/lookup/suppl/doi:10.1073/pnas.2209146119/-/DCSupplemental.

Published September 6, 2022.

low salt solution (50 mM Na^+) at room temperature (7). To help ensure we could resolve partially populated states, we acquired a cryo-EM dataset containing more than 10 million initial particles from ∼40,000 movie stacks, very large compared to other cryo-EM investigations of RNA-only systems, which have typically involved 2 million or fewer particles (11).

Analysis of this cryo-EM single-particle dataset resulted in maps of *Tetrahymena* ribozyme resolved into four conformations, with global map resolutions of 3.53 Å, 3.84 Å, 4.01 Å, and 3.01 Å (Fig. 1*A* and *SI Appendix*, Figs. S1–S3), which we called M1, M2, M3, and N, respectively. We identified the first three conformations as substates of M due to their differences from our previous structure of N, their topological similarity to each other (confirmed by automatic modeling; see below), and the knowledge that the dominant state of the ribozyme under these conditions is M, as defined by folding kinetic experiments read out by onset of functional activity (7, 12–15). We identified the fourth conformation as N because of its near identity (cross-correlation coefficient = 0.94) with a cryo-EM map (EMD-31385) we reported previously for the native *Tetrahymena* ribozyme (prepared to be dominantly in the N state through refolding the RNA at 50 °C). Under the current refolding condition, the majority of the *Tetrahymena* ribozymes in our particle images are M1 (40.8%), followed by M2 (21.0%), M3 (8.9%), and N (29.3%), resulting from the final 3D classification (Fig. 1*A* and *SI Appendix*, Fig. S2). Not all the particles were used toward the final reconstruction, and there are apparent and subtle structural variations among particles within the final classes based on the image processing protocol we adopted (*SI Appendix*, Fig. S2). Therefore, it is likely that there are additional substates that we are not able to distinguish with the current method of analysis. We present and discuss here the maps of M1, M2, M3, and N with distinctly different conformations.

Each of these maps displays a highly similar conformation, except within the catalytic core region. The three M maps have different arrangements of the catalytic core elements compared to the N state, and the three M maps are also subtly different from each other in this region (Fig. 1*A*). As further illustration of the core flexibility in M, the local map resolutions within the M1, M2, and M3 maps are lower in the catalytic core compared to the periphery (Fig. 1*B*). As a final illustration of flexibility in M substates, the overall resolutions of the M substates could not be refined to better than 3.5 Å (*SI Appendix*, Figs. S2 and S3). In contrast, the N state could be resolved to a better resolution of 3.0 Å as defined by Fourier shell correlation(*SI Appendix*, Fig. S3*A*) and local voxel resolution maps (Fig. 1*B*), despite involving a smaller subset of the particles than the M1 substate.

M Has a Nonnative Catalytic Core. Automated DRRAFTER coordinate building into the four cryo-EM maps (16), followed by model optimization with Coot (17) and Phenix (18), enables more detailed structural comparisons between M and N states. While not at the atomically detailed level due to the moderate resolutions of M1, M2, and M3 maps, the convergence in core topologies from independent DRRAFTER modeling runs (*SI Appendix*, Fig. S4*A*) and visual confirmation of the model fits into the density gave us confidence in the relative arrangements of all strands and helices in the final refined models (Movie S1). The convergence, or average pairwise root-mean-square deviation,

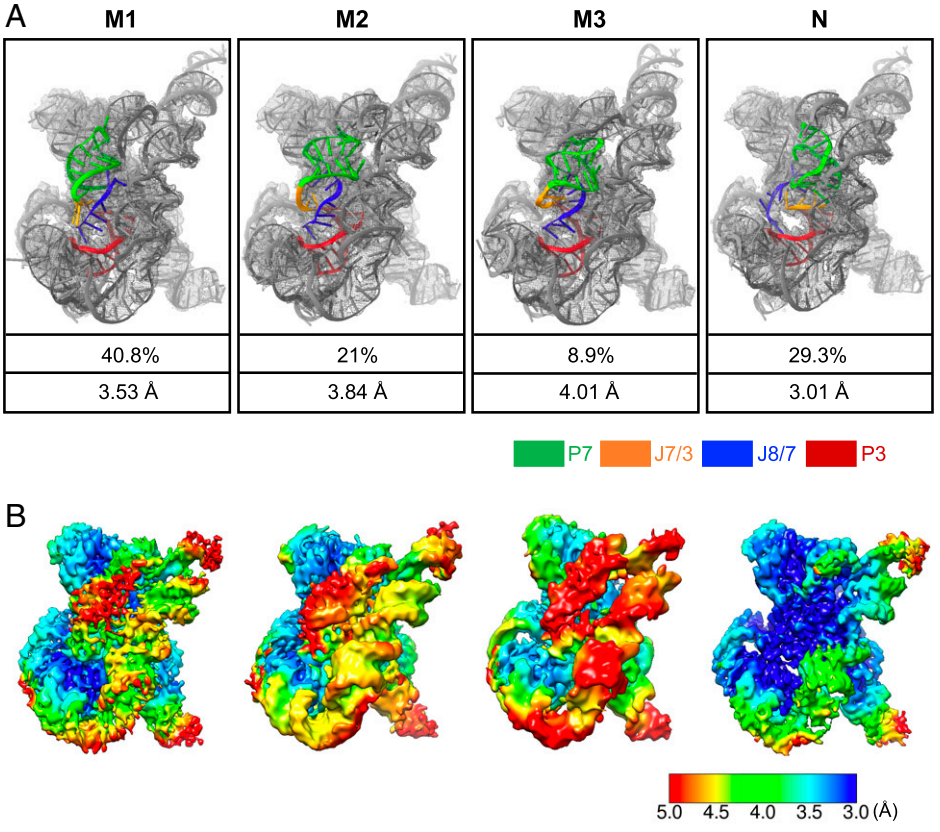

Fig. 1. Structures of *Tetrahymena* ribozyme folded at room temperature, revealed by cryo-EM. (*A*) Reconstructed cryo-EM maps and atomic models of *Tetrahymena* ribozyme folded at room temperature. Ribozyme was prepared in a low-salt solution (50 mM Na^+) at room temperature, and samples were frozen 15 min after addition of 10 mM $MgCl_2$ to promote tertiary folding. The percentages and resolutions in the last two rows refer to the final dataset and final maps. (*B*) Resolution maps for the final 3D reconstructions of *Tetrahymena* ribozyme.

of the 10 best-scoring models has previously been shown to correlate with modeling accuracy (16) and suggests that our models are realistic representations of the M substates (*SI Appendix*, Fig. S4*A*). Furthermore, our models match well with the density, with the indication of regions with good and poor resolvability as measured by the Q-scores (19) (*SI Appendix*, Fig. S4*B*).

As has been previously confirmed with chemical probing and fluorescence experiments (7), the secondary structures (Watson–Crick base pairing pattern) of M1, M2, M3, and N are identical, including the presence of P3 and P7 Watson–Crick-paired helices in the ribozyme core (Fig. 2). In particular, alternative secondary structure pairings that are known to occur in early ribozyme folding intermediates like the unfolded state are replaced by native secondary structure pairings in the late folding intermediates M and N, consistent with our data (7, 20). In addition, their tertiary structures are also highly similar, except the catalytic core (Fig. 2 and *SI Appendix*, Figs. S5 and S6). All the structures have four single-stranded junctions within the core region (J3/4, J6/7, J7/3, and J8/7). However, the J7/3 and J8/7 strands in the M structures cross each other very differently from those in N (Fig. 2 and Movie S1). In the N structure, J8/7 originates from P8 and passes "behind" both the P7 helix and J7/3. In all three M structures, J8/7 remains behind P7 but passes in front of J7/3 (Fig. 2 and *SI Appendix*, Fig. S5 and Movies S1 and S2).

Along with the extensive structural rearrangements of J7/3 and J8/7, their immediately connected regions, especially P7, exhibit conformational changes (Fig. 2). The strand crossing of J7/3 and J8/7 precludes the P7–purine-rich interaction that has been discovered recently for N (Fig. 3) (6). Indeed, without the P7–purine-rich interaction, P7 is flexible, as indicated in the local voxel resolution maps (Fig. 1*B*); shifts in its position and orientation are the largest differences between the M1, M2, and M3 substates (*SI Appendix*, Fig. S5*B*) (7). Strand J6/7, helices P6b and P8, and some peripheral domains such as P5b and P9.2 also exhibit moderate conformational shifts (*SI Appendix*, Figs. S5 and S6), which possibly stem from their inherent flexibility,

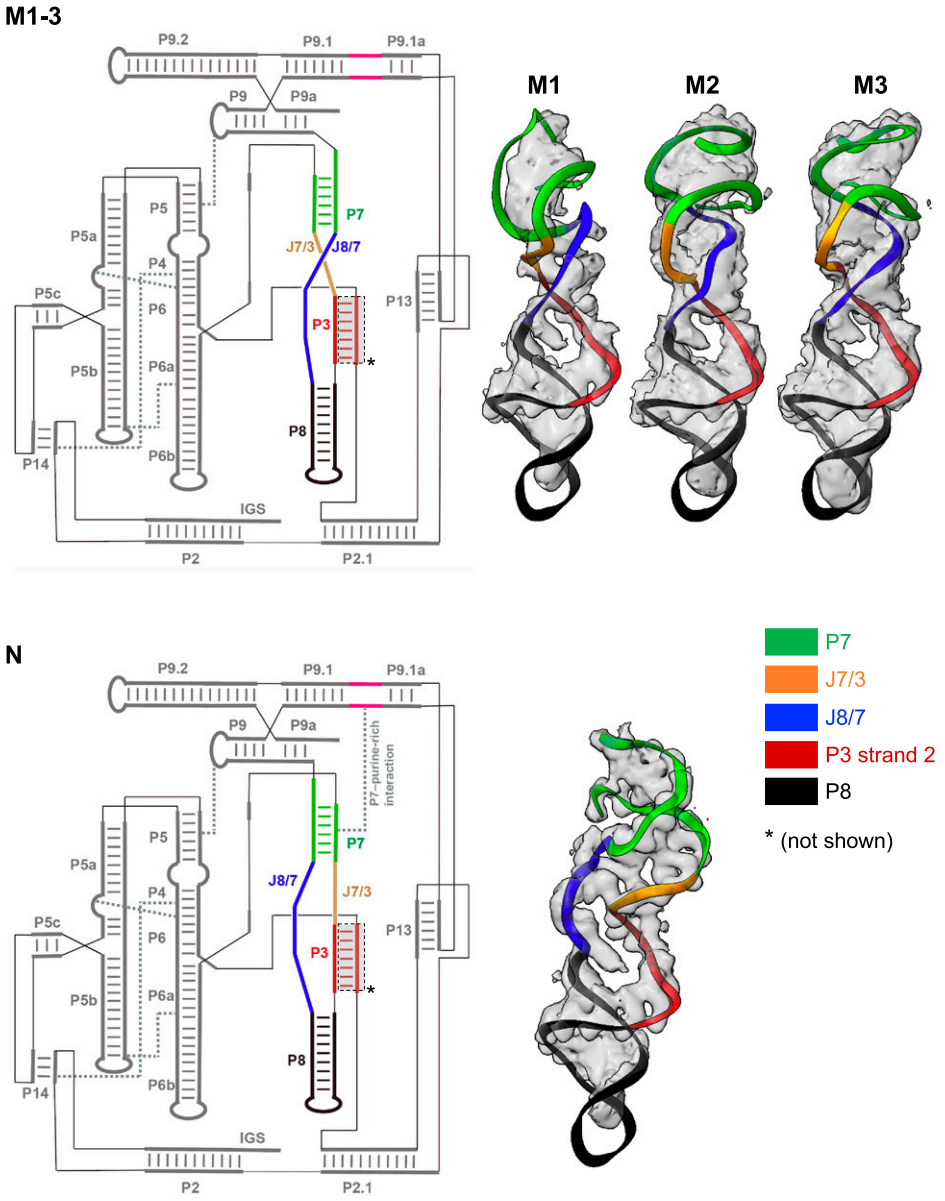

Fig. 2. Topological difference between M and N. M and N adopt identical secondary structures but distinct tertiary structures. The secondary structure diagrams are drawn to highlight changes in the core strand crossing. Close-up views show the 3D models fitted to cryo-EM densities, again emphasizing the topological difference between M and N. For clarity, the first strand of the P3 helix is not shown in 3D models. Secondary structure diagrams were adapted from RiboDraw (https://github.com/ribokit/RiboDraw) and made with Adobe Illustrator. Main tertiary contacts are shown as gray dashed lines.

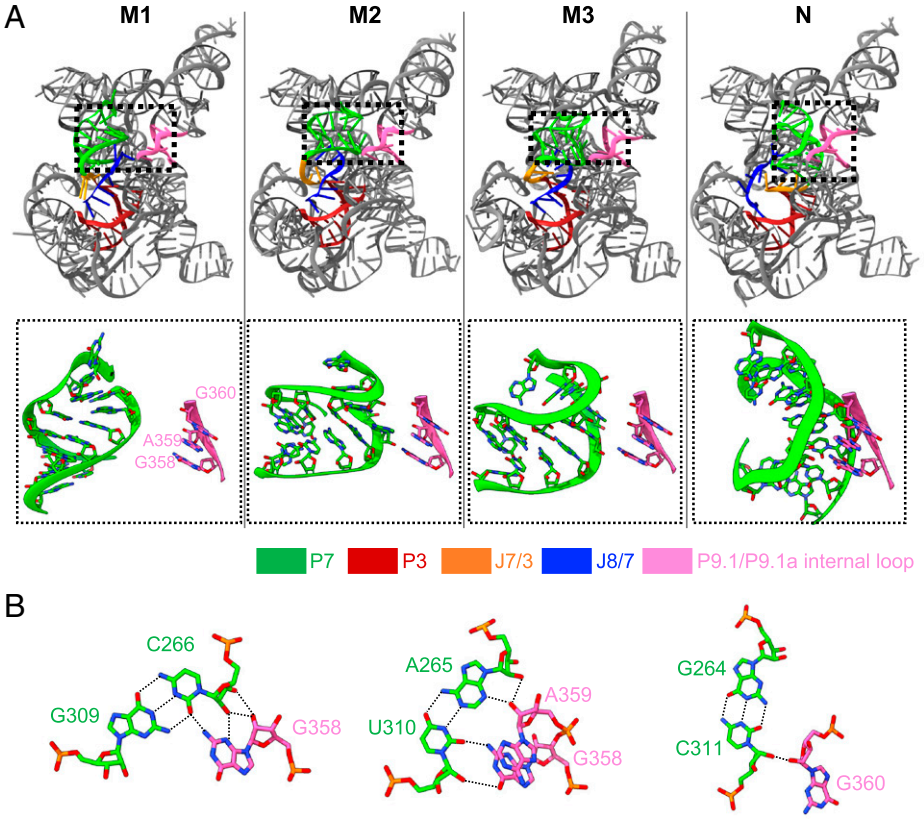

Fig. 3. Absence of P7–purine-rich interaction in M substates. (*A*) G358, A359, and G360 of the loop connecting P9.1 and P9.1a interact with the minor groove of P7 to form the P7–purine-rich interaction in N, which is missing in M due to local structural rearrangements. (*B*) The detailed H-bond interactions between P7 and P9.1 in the N state are shown. Dashed lines, hydrogen bonds.

also reflected by local voxel resolution maps and poorer Q scores (Fig. 1*B* and *SI Appendix*, Fig. S4*B*) and structural changes in the catalytic core. These data are in accord with prior chemical probing data (7, 9) that showed changes in backbone reactivity to hydroxyl radicals in M relative to N restricted mainly to the P7 region with minor changes in P6b and P8 and changes in base reactivity to dimethyl sulfate and inline hydrolysis restricted to strands in the ribozyme core and in the purine-rich internal loop of P9.1, the partner of P7 in the P7–purine-rich interaction (6). Overall, the M state is very similar to N but has a nonnative catalytic core, with the most striking feature being the rotated P7 helix attached to two "miscrossed" J7/3 and J8/7 strands.

Insights into the Mechanism of Transit from M to N. The differences observed in our structures provide an explanation for the very slow refolding (hours to days) of M to N states and confirm a topological isomer model previously proposed on the basis of biochemical experiments (3, 7–10). On one hand, all four structures we have solved are quite similar. Indeed, the similarity of M1, M2, and M3 and the feasibility of simple motions in their core elements like P7, J7/3, and J8/7 to transition from one to the other structures (Movie S2) support their identification as substates of the single state M previously identified through biochemical experiments. However, the M substates are different from N in this respect. The crossing of J7/3 and J8/7 makes a direct motion between any of the M substates to N stereochemically impossible. Stated differently, if only P7, J7/3, and J8/7 are allowed to move, they would have to pass through each other to transit from M to N (Fig. 4 and Movie S3).

This topological barrier means that transiting from M to N must necessarily require significant movement of elements beyond P7, J7/3, and J8/7, but the other elements are held into place by connections to other ribozyme elements that are themselves anchored into place by peripheral tertiary contacts. Therefore, any pathway that allows the M core topology to shift to the N core topology requires at least one secondary structure element or peripheral tertiary contact to be broken, and many such contacts may need to be broken to allow enough space for the motions needed to change core topologies. Such breaking of stable tertiary contacts is expected to be slow, providing an explanation for the paradoxically long lifetime of the misfolded kinetic trap M.

An example of a possible M-to-N refolding pathway involves breaking the P3 helix, which is stacked with P7 on one side and with P8 on another side to form the P7–P3–P8 coaxial stack (Fig. 4). Previous mutagenesis and kinetic results have shown that the P3 helix transiently unfolds during the transition from M to N (9). Disruption of P3 would allow P8 to rotate 360°, twisting the J7/3 and J8/7 strands into their correct positions (Movie S3). Reformation of P3 and rotation of P7 180° would enable P7 to pack in against the P9.1–P9.2 helical stack, forming the P7–purine-rich interaction and achieving the native topology. In order to allow P3, P7, and P8 to make these large conformational changes, it is probably necessary to transiently break one or more of the peripheral tertiary contacts that cage these functionally important elements into the core. For example, disruption of the L9–P5 interaction, which could restrict P7 movement, or the P13 pseudoknot, which anchors the P9.1 helix containing the purine-rich internal loop, could grant this region of the ribozyme the flexibility needed to transition from M to N.

For all refolding pathways, any factors that promote transient breaking of peripheral tertiary contacts, such as L9–P5, P13,

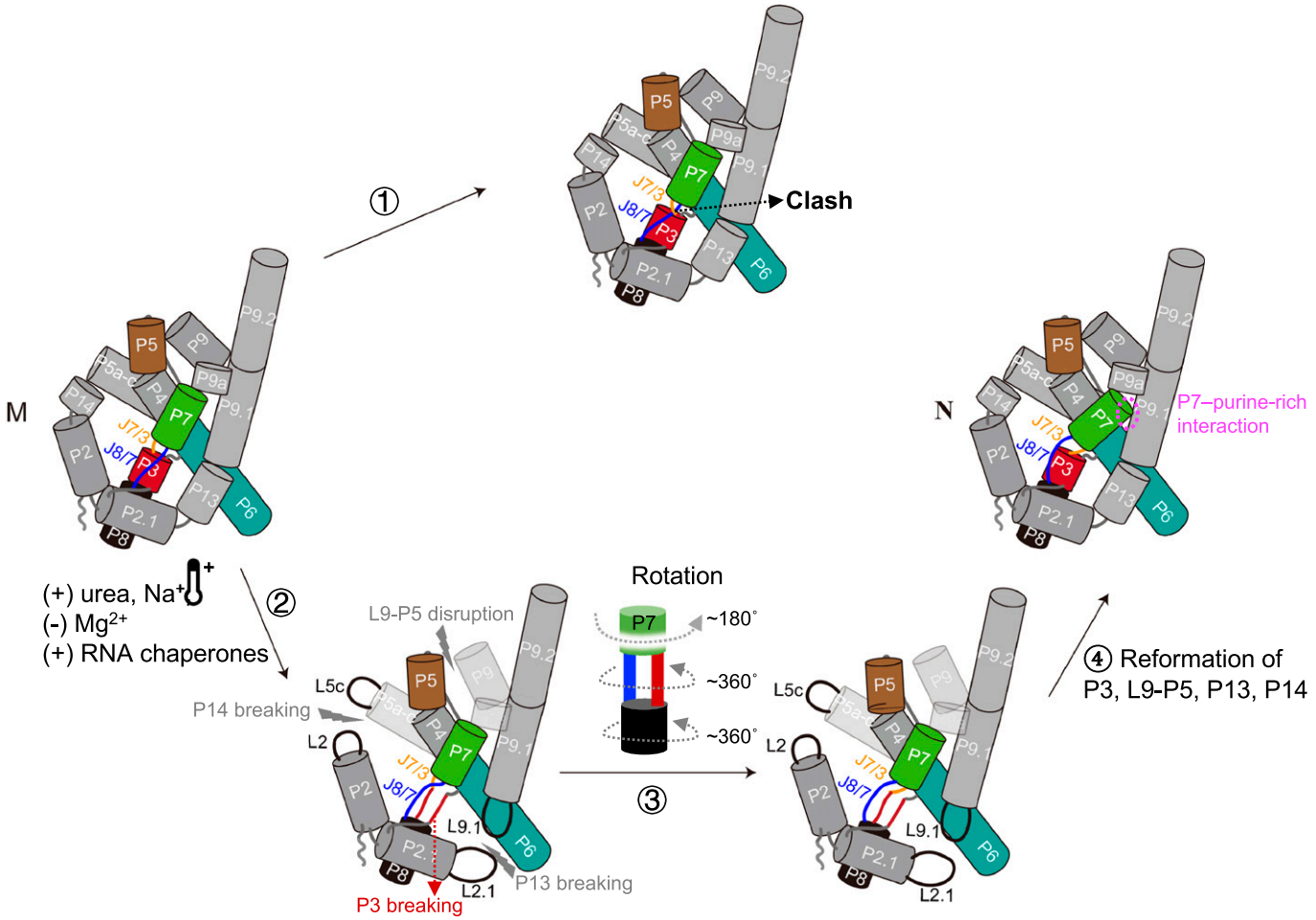

Fig. 4. A possible M-to-N refolding pathway involves disruption of the P3 helix and peripheral tertiary contacts. During the transition from M to N, the crossing of J7/3 and J8/7 makes the direct transition from M to N stereochemically impossible (1). A possible M-to-N refolding pathway involves the transient breaking of P3 and peripheral tertiary contacts (e.g., L9–P5, P13, P14), which can be regulated by many factors (2). These transient breakings would allow P8 to rotate, turning J7/3 and J8/7 into their correct positions (3). P3 reformation and P7 rotation would enable P7 to pack in against the P9.1 helix, forming the P7–purine-rich interaction and achieving the native topology (4). In this schematic diagram, helices are shown as cylinders. Translucent peripheral regions refer to loosening of peripheral tertiary structure. The dynamic display of the M-to-N refolding pathway is shown in Movie S3.

and P14, should accelerate refolding of the M state to the N state. Consistent with this picture, the transition is strongly accelerated by urea, increased Na^+, and increased temperature (14), accelerated by direct mutations of any of the peripheral tertiary contacts (3), strongly impeded by the structure-stabilizing Mg^{2+} (7), and accelerated by RNA chaperones that nonspecifically unfold RNA structure (15, 21). In summary, the observation of a topological crossing in the complex core of the *Tetrahymena* ribozyme explains slow refolding and other biochemical observations of the M to N transition.

Discussion

For more than two decades, the *Tetrahymena* ribozyme has been known to fold into a dominant long-lived M conformation, but our understanding of the nonnative structural characteristics of M remains incomplete. Here, taking advantage of the ability of single-particle cryo-EM to computationally sort out highly heterogeneous or flexible samples (22–24), we obtained 3D structures of M and N states of *Tetrahymena* ribozyme from a single specimen, revealing the strand topology and global architecture of M. We provide direct structural evidence that M has a partially native-like core and extensively native-like periphery, except for local rearrangements at the catalytic core involving a rotated P7 helix connected to two single-stranded segments, J7/3 and J8/7, that are crossed (Movie S3). An independent cryo-EM analysis of M and N has been reported as a preprint simultaneously with the preparation of this manuscript; though at lower resolution, those completely independent data further support our structures (25).

Previous biochemical studies have demonstrated that M does not significantly cleave the 5′-splice site oligonucleotide substrate and indicated that some local rearrangements prevent the P1 helix, formed by 5′-internal guide sequence and substrate, from docking to the catalytic core, resulting in a significant reduction in enzymatic activity (7, 12–14). J8/7 is a highly conserved junction among group I ribozymes and is part of the catalytic core. During the self-splicing of the *Tetrahymena* ribozyme, two conserved adenosines (A301 and A302) at the 5′-end of J8/7 directly interact with the P1 helix (6, 26–29). Our structures reveal that the J8/7 rearrangement in M disrupts the binding site of the P1 helix, providing direct structural explanations for previous biochemical data. Interestingly, M has been shown to be partially functional; it can cleave a 3′-splice site substrate, indicating that it can populate an intact active site that allows phosphoryl transfer (7). Despite nearby structural changes, the high flexibility of M's active site revealed by our structures (Fig. 1*B* and *SI Appendix*, Fig. S4*B*) may

promote the 3′-splice site mimic binding at the guanosine-binding site in P7, which may account for the partial catalytic activity of ribozyme.

Importantly, our cryo-EM structures confirm key structural predictions of models based primarily on extensive biochemical experiments. Prior chemical probing and mutational analysis indicated that M and N share the same secondary structure and five previously known peripheral tertiary contacts, and cryo-EM confirms this extensive structural similarity. Interestingly, it is known that at equilibrium, N is several kcal/mol more stable than M, but it has been unclear how states with such similar structures could have different stabilities. Our analysis reveals that, compared to N, M is missing a tertiary contact called the P7–purine-rich interaction (Fig. 3). This interaction was not known before recent cryo-EM analysis (6) but may account for the additional stability of N compared to M. Our structures suggest that mutational disruption of the P7–purine-rich interaction should impact the relative thermodynamic stability of M and N, a prediction that might be tested with detailed biochemical analysis (30). In addition, prior data could not distinguish between the possibility that M is a single structure or is an ensemble of 3D structures that interconvert more quickly than the time scale for M-to-N refolding. Our measurements and unbiased classification and modeling have resulted in three structural substates of M, which each yield high-resolution, stereochemically reasonable reconstructions. It will be interesting to test whether M1, M2, and M3 can be kinetically resolved as discrete states through spectroscopic methods like FRET, with probe placement guided by these separate cryo-EM structures.

Most strikingly, the prior model proposed, based on the very slow M-to-N refolding, that the difference between M and N is a topological crossing of at least one pair of strands in the core (7). The ribozyme's ring of peripheral tertiary contacts would trap such a core strand crossing, which prevents a rapid kinetic pathway for M to transit to N. Here, we confirm that such a topological difference exists between M and N and pinpoint the crossing to involve the J7/3 and J8/7 core strands. This specific crossing was not anticipated in prior studies because J7/3 was not considered a potentially movable core strand in previous modeling, illustrating the importance and utility of unbiased cryo-EM structural analysis to reveal important features. These cryo-EM structures suggest possible pathways in transitioning from M to N and may enable experimental tests of these pathways through structure-guided design of mutations, antisense oligonucleotides, small molecules, or crosslinks that favor or trap specific topologies. Such structure-informed constructs and reagents may also allow the dissection of misfolding and refolding in the context of helicases in vitro (15), in cells (31), or even during the group I intron's "life cycle" in *Tetrahymena thermophila*, which has been difficult to study. Interestingly, topologically complex structures have been designed into synthetic RNA nanostructures (32) and have been proposed to be modulated by preexisting secondary structures and cotranscriptional folding for not only the *Tetrahymena* and other group I ribozyme (3, 7, 20, 33, 34) but also other natural RNA systems like SARS coronavirus frameshifting elements (35–37). Other natural RNA misfolding events (e.g., in ribosome biogenesis (38–40)) may also involve topological isomers, but the relevant regions have not yet been visualized with sufficient resolution to discern such crossings. As its application to conformationally heterogeneous molecules continues to advance, we expect cryo-EM to be a critical tool for exploring such biologically interesting topological complexity across RNA systems.

Materials and Methods

RNA Sample Preparation. The DNA template for transcription of L-21 ScaI ribozyme was amplified from the pT7L-21 plasmid with forward primer 5′-TTCTAATACGACTCACTATAGGAGGGAAAAGTTATCAGGCATGCACCTGGTAGC-3′ and reverse primer 5′-ACTCCAAAACTAATCAATATACTTTCGCATACAAATTAGTTCCCAGCGGC TCC-3′. RNA was prepared with the TranscriptAid T7 High Yield Transcription Kit (Thermo Scientific) according to the manufacturer's protocol, and the transcription products were isolated with RNA Clean and Concentrator-25 columns (Zymo Research). RNA was mixed with a buffer containing 95% formamide, 10 mM EDTA, and 0.01% (wt/vol) each bromophenol blue and xylene cyanol and polyacrylamide gel electrophoresis purified on a 10% 29:1 acrylamide:bis, 7 M urea polyacrylamide gel. RNA samples were heated at 90 °C for 3 min before loading, and the gel was run at 25 W until the xylene cyanol dye reached the bottom. The gel was then visualized briefly with a 254-nm UV lamp, and RNA was eluted from the gel with the ZR small-RNA PAGE Recovery Kit (Zymo Research) and then ethanol precipitated.

To prepare the sample for cryo-EM, L-21 ScaI ribozyme RNA (20 μM) was denatured in 50 mM Na-HEPES, pH 8 at 90 °C for 3 min and cooled to room temperature for 10 min. Next, $MgCl_2$ was added to a final concentration of 10 mM, and the sample was incubated at room temperature for 15 min, conditions that produce a population of ribozyme that is ∼90% in the M state and ∼10% in the N state (7). The sample was then placed on ice.

Cryo-EM Data Collection. Three microliters of the *Tetrahymena* ribozyme sample were applied onto glow-discharged 200-mesh R2/1 Quantifoil copper grids. The grids were blotted for 4 s and rapidly cryocooled in liquid ethane with a Vitrobot Mark IV (Thermo Fisher Scientific) at 4 °C and ∼100% humidity. The grids were screened with a Talos Glacios cryo–electron microscope (Thermo Fisher Scientific) operated at 200 kV. The grids were imaged in a Titan Krios cryo–electron microscope (Thermo Fisher Scientific) operated at 300 kV at a magnification of 105,000× (corresponding to a calibrated sampling of 0.82 A° per pixel). Micrographs were recorded by EPU software (Thermo Fisher Scientific) with a Gatan K3 Summit direct electron detector, where each image was composed of 30 individual frames with an exposure time of 3 s and a dose rate of 17.1 electrons per second per $A^{°2}$. Finally, 42,382 movie stacks were collected with a defocus range of –1.2 to –2.8 μm.

Image Processing. All micrographs were motion-corrected in MotionCor2 (41), and the contrast transfer function (CTF) was determined in CTFFIND4 (42). All particles were autopicked via the NeuralNet option in EMAN2 (43) and further checked manually. The resulting number of boxed particles was 10,314,332. Then, particle coordinates were imported to Relion (23), where three rounds of 2D classification were performed to remove 2D class averages with poorly resolved features. The selected 4,028,271 particles were imported to cryoSPARC (24) for generating ab initio maps, and one good conformation with obvious RNA features (e.g., helical grooves and strand connectivity) in some subdomains was derived. Starting with this conformation, we performed the nonuniform refinement together with local and global CTF refinement, yielding a map with 3.5-Å resolution from 2,054,418 particles. The catalytic core region was poorly resolved, and therefore heterogeneous refinement was performed to further classify particles, and four conformations were obtained, including three M states and one N state. Final maps were achieved after another round of nonuniform refinement, with resolutions at 3.53 Å, 3.84 Å, 4.01 Å, and 3.01 Å, respectively. The cited resolutions for the final maps were estimated by the 0.143 criterion of Fourier shell correlation curve in cryoSPARC. (More information is in *SI Appendix*, Fig. S2 and Table S1.)

Model Building. The initial models were built in DRRAFTER (16). First, five individual subdomains of the apo L-21 *Tetrahymena* ribozyme (PDB ID: 7EZ0) comprising helices P2–P2.1, P3 and P8, P4–P6, P9.1–P9.2, and P9–P9a were rigidly fitted into the cryo-EM densities of M1–M3 in UCSF Chimera (44). In a first round of DRRAFTER modeling, single-stranded linker regions in junctions and loops from the apo L-21 N model that did not fit well into the maps were rebuilt. The top 10 models produced by DRRAFTER were well converged for the rebuilt nucleotides. These residues were held fixed during a second round of modeling that was performed to build P7, J7/3, and J8/7 into the maps M1–M3. The convergence of the top 10 DRRAFTER models was then calculated to estimate the modeling accuracy for these regions. The top-scoring DRRAFTER models were

manually inspected and further optimized in Coot (17) and Phenix (18). The quality of final models was evaluated by MolProbity (45) and Q-scores (19). Statistics of the map reconstruction and model optimization are summarized in *SI Appendix*, Table S1. All figures were prepared in Chimera (44) or ChimeraX (46).

Data, Materials, and Software Availability. Cryo-EM structures and atomic models have been deposited in the wwPDB OneDep System under EMD accession codes EMD-33425 (47), EMD-33426 (48), EMD-33427 (49), and EMD-33428 (50) and PDB under ID codes 7XSK (51), 7XSL (52), 7XSM (53), and 7XSN (54), respectively.

ACKNOWLEDGMENTS. We thank the Cryo-EM Center at the University of Science and Technology of China and the Stanford-SLAC Cryo-EM Center, supported by the NIH Common Fund Transformative High-Resolution Cryo-Electron Microscopy program (U24 GM129541) for the cryo-EM data collection. This research was supported by NIH grants (P41GM103832 and R01GM079429 to W.C.; R35GM122579 to R.D.; R21 AI145647 to W.C. and R.D.), start-up funding from University of Science and Technology of China (KY9100000032 to K.Z.), and Fundamental Research Funds for the Central Universities (WK9100000044 to K.Z.).

Author affiliations: [a]MOE Key Laboratory for Cellular Dynamics and Division of Life Sciences and Medicine, University of Science and Technology of China, Hefei, Anhui 230027, China; [b]Department of Bioengineering, Stanford University, Stanford, CA 94305; [c]Department of Biochemistry, Stanford University, Stanford, CA 94305; [d]The State Key Laboratory of Biotherapy, Department of Geriatrics and National Clinical Research Center for Geriatrics, West China Hospital, Sichuan University, Chengdu, Sichuan 610044, China; [e]CryoEM and Bioimaging Division, Stanford Synchrotron Radiation Lightsource, SLAC National Accelerator Laboratory, Stanford University, Menlo Park, CA 94025; and [f]Department of Physics, Stanford University, Stanford, CA 94305

1. K. Kruger *et al.*, Self-splicing RNA: Autoexcision and autocyclization of the ribosomal RNA intervening sequence of *Tetrahymena*. *Cell* **31**, 147–157 (1982).
2. D. Herschlag, RNA chaperones and the RNA folding problem. *J. Biol. Chem.* **270**, 20871–20874 (1995).
3. Y. Wan, H. Suh, R. Russell, D. Herschlag, Multiple unfolding events during native folding of the *Tetrahymena* group I ribozyme. *J. Mol. Biol.* **400**, 1067–1077 (2010).
4. M. S. Rook, D. K. Treiber, J. R. Williamson, Fast folding mutants of the *Tetrahymena* group I ribozyme reveal a rugged folding energy landscape. *J. Mol. Biol.* **281**, 609–620 (1998).
5. P. P. Zarrinkar, J. R. Williamson, Kinetic intermediates in RNA folding. *Science* **265**, 918–924 (1994).
6. Z. Su *et al.*, Cryo-EM structures of full-length *Tetrahymena* ribozyme at 3.1 Å resolution. *Nature* **596**, 603–607 (2021).
7. R. Russell *et al.*, The paradoxical behavior of a highly structured misfolded intermediate in RNA folding. *J. Mol. Biol.* **363**, 531–544 (2006).
8. R. Das *et al.*, The fastest global events in RNA folding: Electrostatic relaxation and tertiary collapse of the *Tetrahymena* ribozyme. *J. Mol. Biol.* **332**, 311–319 (2003).
9. D. Mitchell III, I. Jarmoskaite, N. Seval, S. Seifert, R. Russell, The long-range P3 helix of the *Tetrahymena* ribozyme is disrupted during folding between the native and misfolded conformations. *J. Mol. Biol.* **425**, 2670–2686 (2013).
10. D. Mitchell III, R. Russell, Folding pathways of the *Tetrahymena* ribozyme. *J. Mol. Biol.* **426**, 2300–2312 (2014).
11. H. Ma, X. Jia, K. Zhang, Z. Su, Cryo-EM advances in RNA structure determination. *Signal Transduct. Target. Ther.* **7**, 58 (2022).
12. R. Russell, D. Herschlag, New pathways in folding of the *Tetrahymena* group I RNA enzyme. *J. Mol. Biol.* **291**, 1155–1167 (1999).
13. V. L. Emerick, S. A. Woodson, Fingerprinting the folding of a group I precursor RNA. *Proc. Natl. Acad. Sci. U.S.A.* **91**, 9675–9679 (1994).
14. R. Russell, D. Herschlag, Probing the folding landscape of the *Tetrahymena* ribozyme: Commitment to form the native conformation is late in the folding pathway. *J. Mol. Biol.* **308**, 839–851 (2001).
15. H. Bhaskaran, R. Russell, Kinetic redistribution of native and misfolded RNAs by a DEAD-box chaperone. *Nature* **449**, 1014–1018 (2007).
16. K. Kappel *et al.*, De novo computational RNA modeling into cryo-EM maps of large ribonucleoprotein complexes. *Nat. Methods* **15**, 947–954 (2018).
17. P. Emsley, B. Lohkamp, W. G. Scott, K. Cowtan, Features and development of Coot. *Acta Crystallogr. D Biol. Crystallogr.* **66**, 486–501 (2010).
18. P. D. Adams *et al.*, PHENIX: A comprehensive Python-based system for macromolecular structure solution. *Acta Crystallogr. D Biol. Crystallogr.* **66**, 213–221 (2010).
19. G. Pintilie *et al.*, Measurement of atom resolvability in cryo-EM maps with Q-scores. *Nat. Methods* **17**, 328–334 (2020).
20. J. Pan, S. A. Woodson, Folding intermediates of a self-splicing RNA: Mispairing of the catalytic core. *J. Mol. Biol.* **280**, 597–609 (1998).
21. I. Jarmoskaite, P. Tijerina, R. Russell, ATP utilization by a DEAD-box protein during refolding of a misfolded group I intron ribozyme. *J. Biol. Chem.* **296**, 100132 (2021).
22. K. Zhang *et al.*, Cryo-EM structures of *Helicobacter pylori* vacuolating cytotoxin A oligomeric assemblies at near-atomic resolution. *Proc. Natl. Acad. Sci. U.S.A.* **116**, 6800–6805 (2019).
23. S. H. W. Scheres, RELION: Implementation of a Bayesian approach to cryo-EM structure determination. *J. Struct. Biol.* **180**, 519–530 (2012).
24. A. Punjani, J. L. Rubinstein, D. J. Fleet, M. A. Brubaker, cryoSPARC: Algorithms for rapid unsupervised cryo-EM structure determination. *Nat. Methods* **14**, 290–296 (2017).
25. S. L. Bonilla, Q. Vicens, J. S. Kieft, Cryo-EM reveals an entangled kinetic trap in the folding pathway of a catalytic *RNA*. bioRxiv [Preprint] (2022). https:/doi.org/10.1101/2022.04.05.487152 (Accessed 5 April 2022).
26. M. A. Tanner, T. R. Cech, Joining the two domains of a group I ribozyme to form the catalytic core. *Science* **275**, 847–849 (1997).
27. A. M. Pyle, F. L. Murphy, T. R. Cech, RNA substrate binding site in the catalytic core of the *Tetrahymena* ribozyme. *Nature* **358**, 123–128 (1992).
28. J. K. Strauss-Soukup, S. A. Strobel, A chemical phylogeny of group I introns based upon interference mapping of a bacterial ribozyme. *J. Mol. Biol.* **302**, 339–358 (2000).
29. P. L. Adams, M. R. Stahley, A. B. Kosek, J. Wang, S. A. Strobel, Crystal structure of a self-splicing group I intron with both exons. *Nature* **430**, 45–50 (2004).
30. T. H. Johnson, P. Tijerina, A. B. Chadee, D. Herschlag, R. Russell, Structural specificity conferred by a group I RNA peripheral element. *Proc. Natl. Acad. Sci. U.S.A.* **102**, 10176–10181 (2005).
31. S. P. Koduvayur, S. A. Woodson, Intracellular folding of the *Tetrahymena* group I intron depends on exon sequence and promoter choice. *RNA* **10**, 1526–1532 (2004).
32. D. Liu *et al.*, Synthesizing topological structures containing RNA. *Nat. Commun.* **8**, 14936 (2017).
33. S. L. Heilman-Miller, S. A. Woodson, Effect of transcription on folding of the *Tetrahymena* ribozyme. *RNA* **9**, 722–733 (2003).
34. S. Sinan, X. Yuan, R. Russell, The Azoarcus group I intron ribozyme misfolds and is accelerated for refolding by ATP-dependent RNA chaperone proteins. *J. Biol. Chem.* **286**, 37304–37312 (2011).
35. E. P. Plant, J. D. Dinman, Torsional restraint: A new twist on frameshifting pseudoknots. *Nucleic Acids Res.* **33**, 1825–1833 (2005).
36. K. Neupane *et al.*, Structural dynamics of single SARS-CoV-2 pseudoknot molecules reveal topologically distinct conformers. *Nat. Commun.* **12**, 4749 (2021).
37. K. Zhang *et al.*, Cryo-EM and antisense targeting of the 28-kDa frameshift stimulation element from the SARS-CoV-2 RNA genome. *Nat. Struct. Mol. Biol.* **28**, 747–754 (2021).
38. F. R. Ward, Z. L. Watson, O. Ad, A. Schepartz, J. H. D. Cate, Defects in the assembly of ribosomes selected for β-amino acid incorporation. *Biochemistry* **58**, 4494–4504 (2019).
39. X. Liu, H. Huang, K. Karbstein, Blocking a dead-end assembly pathway creates a point of regulation for the DEAD-box ATPase Has1 and prevents platform misassembly. bioRxiv [Preprint] (2021). https://doi.org/10.1101/2021.09.06.459192 (Accessed 6 September 2021).
40. J. H. Davis *et al.*, Modular assembly of the bacterial large ribosomal subunit. *Cell* **167**, 1610–1622.e15 (2016).
41. S. Q. Zheng *et al.*, MotionCor2: Anisotropic correction of beam-induced motion for improved cryo-electron microscopy. *Nat. Methods* **14**, 331–332 (2017).
42. A. Rohou, N. Grigorieff, CTFFIND4: Fast and accurate defocus estimation from electron micrographs. *J. Struct. Biol.* **192**, 216–221 (2015).
43. G. Tang *et al.*, EMAN2: An extensible image processing suite for electron microscopy. *J. Struct. Biol.* **157**, 38–46 (2007).
44. E. F. Pettersen *et al.*, UCSF Chimera–A visualization system for exploratory research and analysis. *J. Comput. Chem.* **25**, 1605–1612 (2004).
45. V. B. Chen *et al.*, MolProbity: All-atom structure validation for macromolecular crystallography. *Acta Crystallogr. D Biol. Crystallogr.* **66**, 12–21 (2010).
46. E. F. Pettersen *et al.*, UCSF ChimeraX: Structure visualization for researchers, educators, and developers. *Protein Sci.* **30**, 70–82 (2021).
47. S. Li *et al.*, Topological crossing in the misfolded Tetrahymena ribozyme resolved by cryo-EM. EMD. https://www.ebi.ac.uk/emdb/EMD-33425. Deposited 14 May 2022.
48. S. Li *et al.*, Topological crossing in the misfolded Tetrahymena ribozyme resolved by cryo-EM. EMD. https://www.ebi.ac.uk/emdb/EMD-33426. Deposited 14 May 2022.
49. S. Li *et al.*, Topological crossing in the misfolded Tetrahymena ribozyme resolved by cryo-EM. EMD. https://www.ebi.ac.uk/emdb/EMD-33427. Deposited 14 May 2022.
50. S. Li *et al.*, Topological crossing in the misfolded Tetrahymena ribozyme resolved by cryo-EM. EMD. https://www.ebi.ac.uk/emdb/EMD-33428. Deposited 14 May 2022.
51. S. Li *et al.*, Topological crossing in the misfolded Tetrahymena ribozyme resolved by cryo-EM. PDB. https://www.rcsb.org/structure/7XSK. Deposited 14 May 2022.
52. S. Li *et al.*, Topological crossing in the misfolded Tetrahymena ribozyme resolved by cryo-EM. PDB. https://www.rcsb.org/structure/7XSL. Deposited 14 May 2022.
53. S. Li *et al.*, Topological crossing in the misfolded Tetrahymena ribozyme resolved by cryo-EM. PDB. https://www.rcsb.org/structure/7XSM. Deposited 14 May 2022.
54. S. Li *et al.*, Topological crossing in the misfolded Tetrahymena ribozyme resolved by cryo-EM. PDB. https://www.rcsb.org/structure/7XSN. Deposited 14 May 2022.